

Multiwavelength study of *Chandra* X-ray sources in the Antennae

D. M. Clark,^{1,2★} S. S. Eikenberry,² B. R. Brandl,³ J. C. Wilson,⁴ J. C. Carson,^{5,6}
C. P. Henderson,⁷ T. L. Hayward,⁸ D. J. Barry,⁷ A. F. Ptak⁹ and E. J. M. Colbert¹⁰

¹*Instituto de Astronomía, Universidad Nacional Autónoma de México, Apdo Postal 877, Ensenada, Baja California, Mexico*

²*Department of Astronomy, University of Florida, Gainesville, FL 32611, USA*

³*Leiden Observatory, Leiden University, PO Box 9513, 2300 RA Leiden, the Netherlands*

⁴*Department of Astronomy, P.O. Box 400325, University of Virginia, Charlottesville, VA 22904, USA*

⁵*Max Planck Institute for Astronomy, Königstuhl 17, D-69117 Heidelberg, Germany*

⁶*Department of Physics and Astronomy, College of Charleston, 58 Coming Street, Charleston, SC 29424, USA*

⁷*Astronomy Department, Cornell University, Ithaca, NY 14853, USA*

⁸*Gemini Observatory, AURA/Casilla 603, La Serena, Chile*

⁹*NASA/GSFC, 8463 Greenbelt, MD 20770-2548, USA*

¹⁰*Department of Physics and Astronomy, Johns Hopkins University, 3400 North Charles Street, Baltimore, MD 21218, USA*

Accepted 2010 August 5. Received 2010 August 4; in original form 2010 July 14

ABSTRACT

We use Wide-field InfraRed Camera (WIRC) infrared (IR) images of the Antennae (NGC 4038/4039) together with the extensive catalogue of 120 X-ray point sources to search for counterpart candidates. Using our proven frame-tie technique, we find 38 X-ray sources with IR counterparts, almost doubling the number of IR counterparts to X-ray sources that we first identified. In our photometric analysis, we consider the 35 IR counterparts that are confirmed star clusters. We show that the clusters with X-ray sources tend to be brighter, $K_s \approx 16$ mag, with $(J - K_s) = 1.1$ mag.

We then use archival *Hubble Space Telescope* (*HST*) images of the Antennae to search for optical counterparts to the X-ray point sources. We employ our previous IR-to-X-ray frame-tie as an intermediary to establish a precise optical-to-X-ray frame-tie with <0.6 arcsec rms positional uncertainty. Due to the high optical source density near the X-ray sources, we determine that we cannot reliably identify counterparts. Comparing the *HST* positions to the 35 identified IR star cluster counterparts, we find optical matches for 27 of these sources. Using Bruzual–Charlot spectral evolutionary models, we find that most clusters associated with an X-ray source are massive, and young, $\sim 10^6$ yr.

Key words: galaxies: starburst – galaxies: star clusters: general – X-rays: binaries.

1 INTRODUCTION

The numerous X-ray point sources and young, massive star clusters in the Antennae make this galaxy pair an ideal laboratory for studying the environments of X-ray binaries (XRBs). Previously, *Chandra* observations revealed 49 X-ray point sources ranging in luminosity from 10^{38} to 10^{40} erg s^{−1} (Zezas et al. 2002). A 411-ks total exposure, consisting of six additional pointings spread over 2 yr, revealed an additional 71 X-ray sources (Zezas et al. 2006) down to a luminosity of 2×10^{37} erg s^{−1}. While most are XRBs with either a black hole or neutron star, those sources with $L_X > 10^{39}$ erg s^{−1} are more unusual objects classified as ultraluminous X-ray sources

(ULXs). Some theories suggest these ULXs are intermediate mass black holes with masses from 100 to 10 000 M_\odot (e.g. Fabbiano 1989; Zezas, Georgantopoulos & Ward 1999; Makishima et al. 2000; Roberts & Warwick 2000), but there remains a considerable amount of controversy concerning their origins (e.g. King et al. 2001; Roberts 2007 and references therein).

For this study, we use a distance to the Antennae of 19.3 Mpc (for $H_0 = 75$ km s^{−1} Mpc^{−1}), as determined by the spectroscopic redshift (Zezas et al. 2006). However, there exists some ambiguity concerning the distance to this galaxy pair. While a distance derived from the Type Ia supernova 2007sr suggests a distance of 22 ± 3 Mpc (Schweizer et al. 2008), analysis of the red giant branch colours indicate that the distance can range from 22 Mpc to as low as 13.8 Mpc (Saviane, Hibbard & Rich 2004). While this lower distance would halve our luminosity and mass estimates, this factor of a few will not affect any statistical study of their population.

★E-mail: dmclark@astro.unam.mx

Hence, we do not anticipate these discrepancies in the distance to NGC 4038/4039 as being problematic.

Compact objects tend to be associated with massive star formation, which some theories suggest is predominant in young stellar clusters (Lada & Lada 2003). In previous work on the Antennae we find a close association between compact objects and clusters, identifying 15 possible infrared (IR) counterparts to X-ray sources (Clark et al. 2007). Many of these counterparts reside in the spiral arms and ‘bridge’ region of the Antennae – locations predominant in massive star formation. The spiral arms wrap around the northern nucleus and extend to the south of the southern nucleus, while the bridge region is the dense area connecting the two galaxies. Those X-ray sources without counterparts could be compact objects that escaped their parent cluster or remained behind after their cluster dissolved. In Clark et al. (2007) we suggest a third possibility, that some X-ray sources do have counterparts, but these are too faint to see in the IR images.

In this paper, we expand on our initial study by searching for IR counterparts to the 120 X-ray sources identified in Zezas et al. (2006). We then extend this work to optical wavelengths using *Hubble Space Telescope* (*HST*) images of the Antennae. The higher sensitivity of *HST* in non-dust obscured regions allows us to search for additional counterparts to X-ray sources. In addition, combining multiband photometry in the optical and IR, we can use spectral evolutionary models to measure cluster properties. In Section 2 we discuss our IR observations and analysis of optical *HST* archival images. We describe our photometric analysis of counterpart cluster properties in Section 3 and summarize our results in Section 4.

2 OBSERVATIONS AND DATA ANALYSIS

2.1 Infrared and optical imaging

We base this study on near-IR and optical *HST* images of the Antennae. We report the reduction and analysis of the near-IR images in Brandl et al. (2005). In summary, we acquired 20-min total exposures in the *J* (1.25 μm) and *K_s* (2.15 μm) filters using the Wide-field InfraRed Camera (WIRC) on the Palomar 5-m telescope during the night of 2002 March 22. We obtained the optical *HST* images from the literature (Whitmore et al. 1999). This data set was acquired using the Wide-Field Planetary Camera 2 (WFPC2) camera and consists of images in the following filters: *F336W(U)*, *F439W(B)*, *F555W(V)* and *F814W(I)*.

In our efforts to understand the environments of the Antennae X-ray sources, we made frame-ties across three wavelength regimes: *Chandra* X-ray, WIRC IR and *HST* optical images. Using the IR as an intermediary between the optical and X-ray frame-tie has many advantages over direct optical/X-ray matches. First, the IR penetrates dust in similar ways to X-rays, facilitating the identification of counterparts to X-ray sources. Furthermore, while bright IR sources may be obscured in the optical, the converse is generally untrue – any bright *HST* source shows up prominently in the IR images, enabling an excellent optical/IR frame-tie, and thus closing the astrometric loop at all wavelengths. Previous attempts to match X-ray and optical positions produced many possible counterparts, but with poor reliability – as many as 75 per cent of the matches are chance coincidences (Zezas et al. 2002).

In the new catalogue of X-ray sources, Zezas et al. (2006) revised the X-ray source positions and the new positions differ by 0.2 ± 0.4 arcsec in right ascension (RA) and 0.6 ± 1.8 arcsec in declination (Dec.) as compared to those coordinates listed in Zezas et al. (2002). Considering we are searching for IR counterparts within 1 arcsec of

an X-ray source position (see below), we adjusted our initial frame-tie (Clark et al. 2007) between the WIRC IR *K_s*-band image and the X-ray sources listed in Zezas et al. (2002), to account for the new, X-ray coordinates listed in Zezas et al. (2006). This modification to the initial frame-tie yielded the same rms positional uncertainty, ~ 0.5 arcsec.

Once our frame-tie between the IR and X-ray was in place, we extrapolated X-ray positions to optical *HST* *I*-band positions. Tying *Chandra* X-ray coordinates directly to *HST* positions is non-trivial due to field crowding in the *HST* images. Instead, we used our excellent frame-tie between the IR and X-ray as an intermediary. Selecting only bright, isolated optical sources, we made our frame-tie using 12 targets corresponding to sources seen in the IR. Using the mapping method describe above, we matched IR pixel positions to *HST* RA and Dec. This frame-tie yielded an rms positional uncertainty of less than 0.6 arcsec. Applying our IR-to-optical astrometric fits to previously derived *K_s*-band, *x,y* pixel positions of X-ray sources (Clark et al. 2007), we found the *HST* positions for all *Chandra* X-ray sources.

2.2 Identification of infrared counterparts to *Chandra* Sources

Once our astrometric frame-tie was in place, we found a total of 28 likely and 10 possible IR counterparts to *Chandra* X-ray sources in the Antennae, where likely counterparts are defined to be within a 1.0 arcsec radius (equivalent to twice the positional uncertainty for our frame-tie) of an X-ray source and possible counterparts are between 1.0 and 1.5 arcsec (four to six times the positional uncertainty) from an X-ray source. The 35 sources that are confirmed star clusters are listed in Table 1 and shown in Fig. 1, with subimages of each source displayed in Fig. 2. As can be seen in the figure, the counterparts are almost exclusively in the spiral arms and bridge region. Of the 38 X-ray sources with counterparts, two are the nuclei (X-50 and X-61 as listed in table 5 of Zezas et al. 2006), one is a background quasar (X-90; Clark et al. 2005) and two lack measured X-ray luminosities (X-24 and X-52). The source X-107 is on the edge of the frame, making sky subtraction difficult, so we excluded it. Therefore, in our analysis of cluster properties, we only considered the 32 IR counterparts that are confirmed star clusters and that have X-ray sources with measured luminosities. Furthermore, of the 15 IR cluster counterparts found in Clark et al. (2007), four drop out as counterparts in this new analysis – the X-ray sources X-10, X-26, X-15 and X-22, following the numeration in table 1 of Zezas et al. (2002), are no longer associated with a star cluster.

Using the technique developed in Clark et al. (2007), which is based on the IR source density in the field around each X-ray source position, we attempted to estimate the level of ‘contamination’ of these counterpart samples due to chance superpositions of unrelated X-ray sources and IR clusters. We expect eight sources with a 1σ uncertainty of $+0.1/-0.1$ ¹ of the 28 likely counterparts to be due to chance superpositions of unrelated objects, and 10 with a 1σ uncertainty of $+0.4/-0.3$ ¹ for the 10 possible counterparts to be chance superpositions.

In Fig. 3 we plot the X-ray luminosity versus the separation in arcseconds to the associated IR cluster counterpart. We also divided the X-ray sources into three luminosity bins: low luminosity X-ray sources (LLXs) had $L_X < 3 \times 10^{38} \text{ erg s}^{-1}$, high luminosity X-ray sources (HLXs) were between L_X of 3×10^{38} and $1 \times 10^{39} \text{ erg s}^{-1}$,

¹ Found using confidence levels for small number statistics listed in tables 1 and 2 of Gehrels (1986).

Table 1. IR cluster counterparts to *Chandra* X-ray sources. $\Delta\alpha$ and $\Delta\delta$ are the positional offsets in units of arcsec from the *Chandra* coordinates to the WIRC coordinates of the proposed counterpart. *Chandra* Src ID numbers follow the naming convention of Zezas et al. (2006). The listed RA and Dec. *Chandra* coordinates have an uncertainty of 0.5 arcsec (Zezas et al. 2006). The near-IR J and K_s magnitudes were measured using PSF photometry. The values in parenthesis for each magnitude are uncertainties in the final listed digit.

| <i>Chandra</i> Src ID | RA | Dec. | $\Delta\alpha$ (arcsec) | $\Delta\delta$ (arcsec) | J | K_s |
|-----------------------|-------------|--------------|-------------------------|-------------------------|-------------|-------------|
| Likely counterparts | | | | | | |
| 7 | 12:01:49.64 | −18:52:07.10 | 0.45 | 0.66 | 19.93(0.21) | 18.88(0.18) |
| 11 | 12:01:50.35 | −18:52:15.50 | 0.30 | 0.76 | 16.47(0.02) | 15.89(0.02) |
| 16 | 12:01:50.51 | −18:52:04.30 | 0.15 | 0.08 | 16.21(0.01) | 15.66(0.02) |
| 22 | 12:01:51.01 | −18:52:33.00 | 0.45 | 0.55 | 17.56(0.02) | 16.59(0.01) |
| 24 | 12:01:51.14 | −18:52:31.70 | 0.15 | 0.18 | 17.56(0.02) | 16.59(0.01) |
| 27 | 12:01:51.32 | −18:52:25.40 | 0.45 | 0.42 | 18.27(0.01) | 17.37(0.08) |
| 38 | 12:01:52.02 | −18:52:27.50 | 0.60 | 0.30 | 16.82(0.01) | 16.10(0.01) |
| 47 | 12:01:52.75 | −18:51:30.10 | 0.15 | 0.09 | 18.48(0.04) | 17.78(0.02) |
| 51 | 12:01:53.00 | −18:52:09.10 | 0.75 | 0.04 | 15.77(0.01) | 15.13(0.06) |
| 52 | 12:01:53.08 | −18:52:23.80 | 0.60 | 0.52 | 17.16(0.02) | 16.21(0.01) |
| 58 | 12:01:53.41 | −18:53:07.00 | 0.45 | 0.20 | 15.79(0.18) | 15.51(0.10) |
| 60 | 12:01:53.42 | −18:53:51.30 | 0.45 | 0.62 | 21.95(1.68) | 17.97(0.09) |
| 83 | 12:01:54.50 | −18:53:06.70 | 0.00 | 0.57 | 16.71(0.08) | 16.45(0.07) |
| 84 | 12:01:54.56 | −18:53:03.80 | 0.15 | 0.00 | 15.05(0.03) | 14.27(0.02) |
| 85 | 12:01:54.62 | −18:52:09.40 | 0.45 | 0.05 | 18.52(0.20) | 16.63(0.01) |
| 86 | 12:01:54.78 | −18:52:52.00 | 0.15 | 0.11 | 16.76(0.02) | 14.88(0.04) |
| 87 | 12:01:54.84 | −18:52:14.80 | 0.15 | 0.25 | 16.60(0.03) | 15.92(0.01) |
| 88 | 12:01:54.98 | −18:53:06.60 | 0.30 | 0.03 | 16.52(0.01) | 14.66(0.01) |
| 91 | 12:01:55.05 | −18:52:41.00 | 0.90 | 0.50 | 17.81(0.01) | 16.89(0.02) |
| 94 | 12:01:55.17 | −18:52:47.90 | 0.45 | 0.09 | 17.10(0.07) | 15.71(0.02) |
| 98 | 12:01:55.54 | −18:52:23.80 | 0.30 | 0.03 | 15.86(0.07) | 15.21(0.04) |
| 99 | 12:01:55.65 | −18:52:15.20 | 0.60 | 0.13 | 16.30(0.04) | 15.40(0.01) |
| 10 | 12:01:55.74 | −18:52:42.70 | 0.15 | 0.57 | 16.70(0.02) | 16.10(0.02) |
| 102 | 12:01:55.74 | −18:52:06.10 | 0.45 | 0.01 | 17.81(0.02) | 17.48(0.02) |
| 107 | 12:01:56.47 | −18:54:42.00 | 0.15 | 0.06 | – | – |
| 117 | 12:01:58.42 | −18:52:49.60 | 0.30 | 0.80 | 17.64(0.02) | 16.90(0.04) |
| Possible counterparts | | | | | | |
| 14 | 12:01:50.47 | −18:52:21.80 | 0.75 | 1.01 | 15.86(0.03) | 15.12(0.02) |
| 15 | 12:01:50.47 | −18:52:12.70 | 1.50 | 0.29 | 14.98(0.02) | 14.06(0.01) |
| 36 | 12:01:51.85 | −18:52:27.80 | 0.75 | 1.25 | 16.77(0.04) | 15.94(0.01) |
| 41 | 12:01:52.19 | −18:52:20.60 | 1.35 | 0.51 | 17.06(0.04) | 16.18(0.02) |
| 81 | 12:01:54.35 | −18:52:10.30 | 1.20 | 0.64 | 20.30(0.45) | 16.84(0.03) |
| 89 | 12:01:54.96 | −18:52:32.50 | 0.15 | 1.19 | 18.11(0.02) | 17.47(0.04) |
| 92 | 12:01:55.06 | −18:52:16.50 | 0.90 | 1.15 | 17.25(0.03) | 15.77(0.01) |
| 95 | 12:01:55.37 | −18:52:48.90 | 0.15 | 1.08 | 16.21(0.02) | 15.27(0.04) |
| 11 | 12:01:59.20 | −18:51:37.30 | 0.60 | 1.01 | 17.78(0.01) | 15.97(0.01) |

while $L_X > 1 \times 10^{39} \text{ erg s}^{-1}$ were ULXs. All luminosities were taken from table 5 of Zezas et al. (2006). Note that there is no trend in separation from the IR cluster counterpart and X-ray luminosity. This seems to indicate no preference as to where XRBs of different luminosity classes form in star clusters.

2.3 Identification of optical counterparts to *Chandra* sources

The complex field seen in the *HST* images of the Antennae makes finding counterparts to X-ray sources difficult and necessitated a different method for defining counterparts than that used for the IR (see above and Clark et al. 2007). Using our precise frame-tie we defined areas of positional uncertainty around each X-ray source, specifically an inner aperture with a radius of 1 arcsec and an annular region of 2.0–3.0 arcsec. We then defined possible matches as those X-ray sources with two optical sources in the circular aperture and

less than five optical sources in the annulus, and likely matches as those X-ray sources with one optical source in the circular aperture and less than five optical sources in the annulus. If more than five sources lay in the annular region, we considered the region to be too complicated for a positive counterpart identification, regardless of how many sources lay in the inner aperture. Using these criteria, we identified seven X-ray sources with likely matches to a single I -band source and one X-ray source, with possible matches to two I -band sources. We used the *HST* I -band image to search for counterparts because this filter covers the longest wavelength of the available *HST* bands and so is least affected by extinction.

Repeating the procedure discussed in Clark et al. (2007), we estimated the level of source contamination associated with our identified optical counterparts to X-ray sources. We expect five with a 1σ uncertainty of $+0.5/-0.3^1$ of the seven likely counterparts to be due to chance superpositions of unrelated objects, and seven with

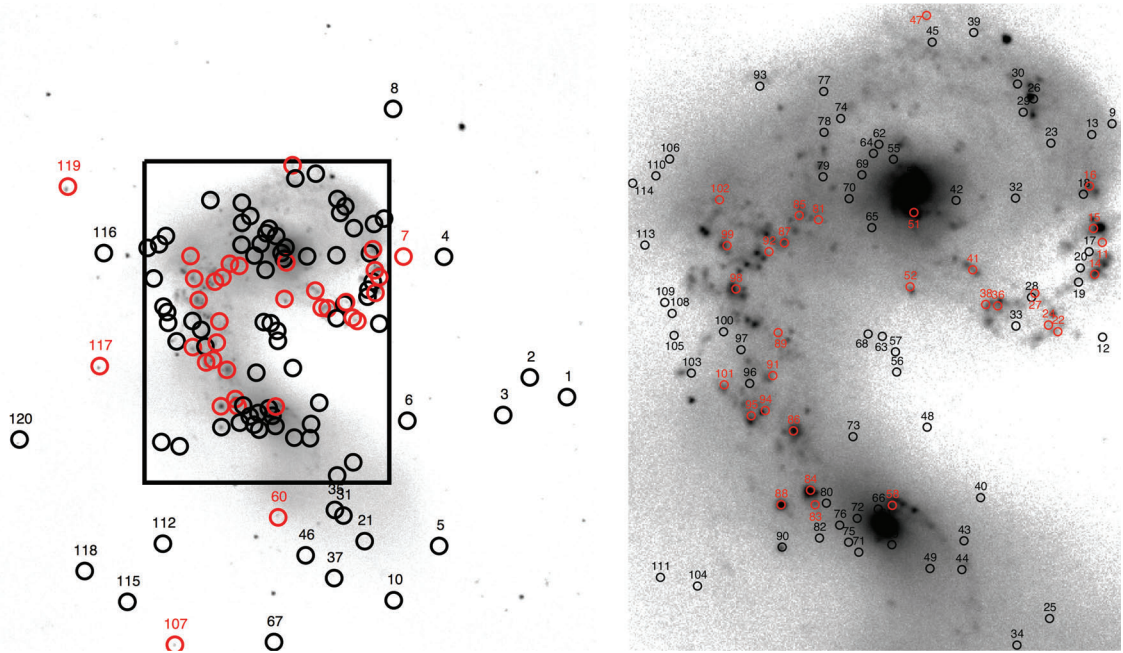


Figure 1. X-ray positions from Zezas et al. (2006) overlaid on the WIRC, K_s -band image of the Antennae. The right-hand panel is a 1.6×2.0 arcmin blow-up of the central regions of the galaxy pair showing the X-ray source positions in more detail. Red circles are those X-ray sources with IR counterparts, while black circles are X-ray sources lacking counterparts.

a 1σ uncertainty of $+3.8/-5.4^1$ for the one possible counterpart to be chance superpositions. Clearly these statistics indicate the majority of our optical counterparts are chance superpositions and further demonstrate the difficulty of making such matches in the complex structure of the *HST* images of the Antennae. Therefore, we did not perform a photometric analysis on these source as we could not reliably identify the counterparts and so could not provide any statistically meaningful information on the X-ray source environments.

Instead, we considered the optical equivalents to the 32 IR cluster counterparts identified in this work. These optical matches were identified using the IR-to-optical astrometric frame-tie to match IR counterpart positions to *HST* positions. As we discuss below, in many cases a single IR counterpart split into multiple optical counterparts, and we labelled these conglomerations as a positive match. We found optical counterparts to 27 IR cluster counterparts and Fig. 2 displays subimages of those counterparts to X-ray sources seen across all six IR and optical bands. Fig. 4 is an *I*-band image of the Antennae showing the positions of all counterpart candidates to X-ray sources.

3 RESULTS AND DISCUSSION

3.1 Photometric properties of the IR counterparts

3.1.1 Colour–magnitude diagrams

We made ($J - K_s$) versus K_s colour–magnitude diagrams (CMDs) using the 226 star clusters with J and K_s magnitudes. The cluster magnitudes for 219 sources were first reported in Clark et al. (2007) and this study includes photometry for an additional seven clusters. Fig. 5 expands on the CMD presented in Clark et al. (2007), by including a larger sample of clusters associated with X-ray sources. As we did previously (Clark et al. 2007), we divided the X-ray sources into the three luminosity classes, LLX, HLX and ULX (see

Section 2.2). As can be seen in the plot, the majority of the X-ray sources with IR counterparts are LLXs, 26, while there are five HLXs and two ULXs. Interestingly, in the new list of X-ray sources (Zezas et al. 2006), three that are associated with IR star clusters in both Clark et al. (2007) and here change in X-ray luminosity class from those published values in Zezas et al. (2002); X-25 goes from HLX to LLX, X-32 from ULX to HLX and X-40 from LLX to HLX. Comparing the old and new sample of IR counterparts, the new sample is about a half a magnitude fainter (see Table 2), but shows no difference in colour compared with our previous study (Clark et al. 2007, table 4).

3.1.2 Cluster mass estimates and η

Following the procedure outlined in Clark et al. (2008), we computed the cluster mass relation, η , defined in that paper, but now included our extended list of clusters with X-ray counterparts. As defined in Clark et al. (2008), η relates the function of X-ray detections per mass as a function of cluster mass and can be formalized with the following equation:

$$N_X(M_c) = N_{Cl}(M_c)\eta(M_c)M_c. \quad (1)$$

The quantity $N_X(M_c)$ is the number of detected X-ray sources with an IR cluster counterpart, $N_{Cl}(M_c)$ is the number of detected clusters and $\eta(M_c)$ is the fraction of X-ray sources per unit mass, all as a function of cluster mass, M_c .

If $\eta(M_c)$ increases or decreases over a range in M_c , this means there could be something peculiar about massive cluster physics to favour or suppress XRB formation. In contrast, a constant $\eta(M_c)$ across all M_c would indicate that more massive clusters are more likely to have an XRB simply because they have more stars.

We estimated cluster mass using K_s -band luminosity, M_{K_s} , but expressed in terms of the observational quantity, flux, F_{K_s} . Given a set of η values plotted against cluster flux, a significant slope

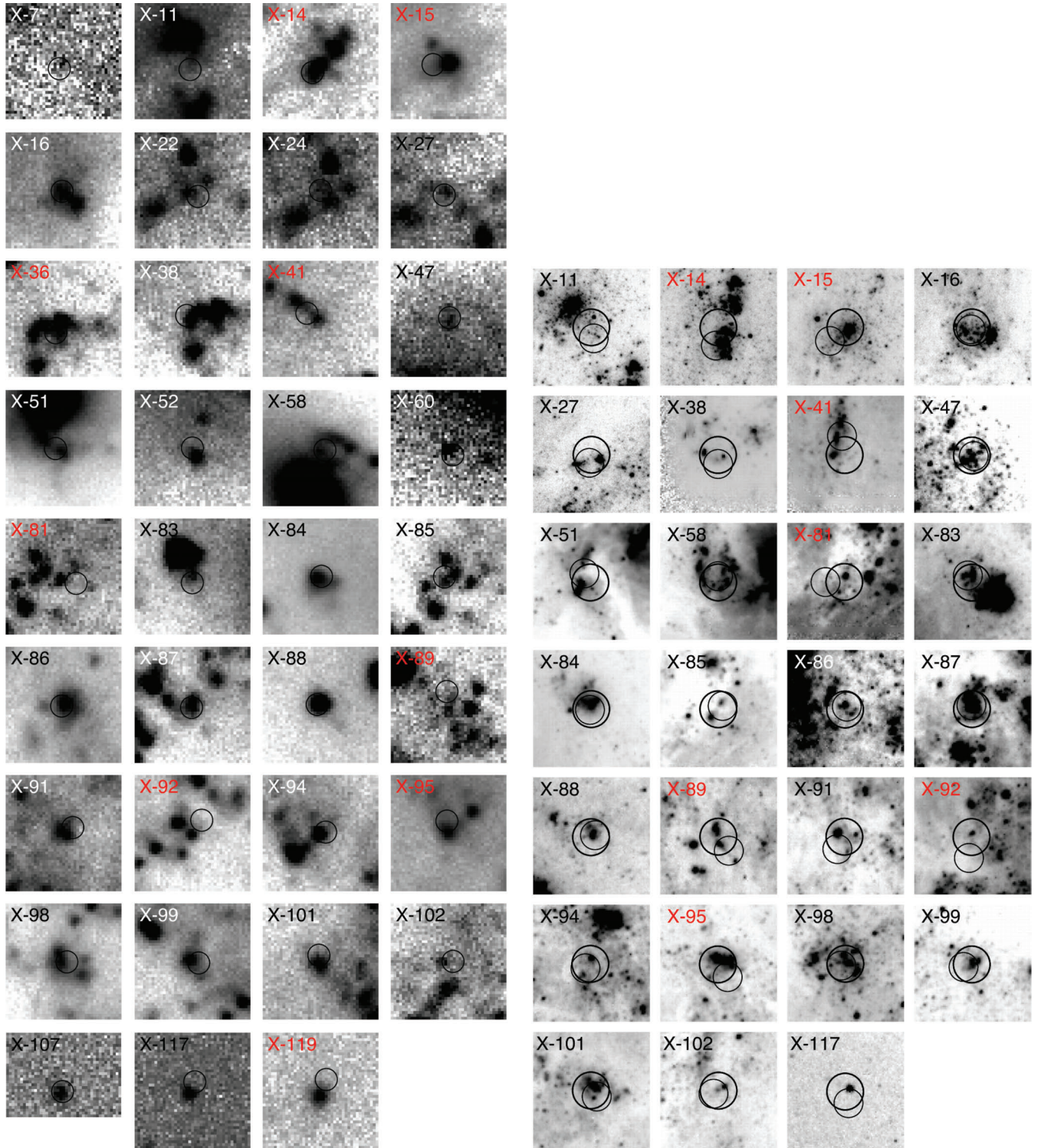


Figure 2. Left-hand panel: subimages from the K_s -band image of the Antennae for X-ray sources with cluster counterparts. Each subimage is 10×10 arcsec, centred on the cluster counterpart and the circles are 1 arcsec in radius, centred on the X-ray source position. X-ray sources labelled in red show possible matches to cluster counterparts. Right-hand panel: subimages highlighting optical counterparts to X-ray sources with IR cluster counterparts. The small circles are positional error circles with 1.0 arcsec radii centred on X-ray source positions. The larger circles are centred on cluster counterparts and have 1.3 arcsec radii equivalent to the K_s -band photometric aperture. We label those X-ray sources with possible counterparts in red. Each image is 6.0×6.0 arcsec.

could indicate an overabundance of X-ray sources in more massive clusters, more than would be expected from simple scaling arguments. Fig. 6 shows $\eta(F_{K_s})$ computed for each cluster, but binned by bins of $F_{K_s} = 4.1 \times 10^6$ data number (DN) $^{-1}$. As can be seen,

there does not appear to be a significant slope and η is consistent with a constant value of $\eta(F_{K_s}) = 5.5 \times 10^{-8}$ with an uncertainty of $\sigma_{\bar{\eta}} = 7.0 \times 10^{-9}$ and is in agreement with the value found in Clark et al. (2008).

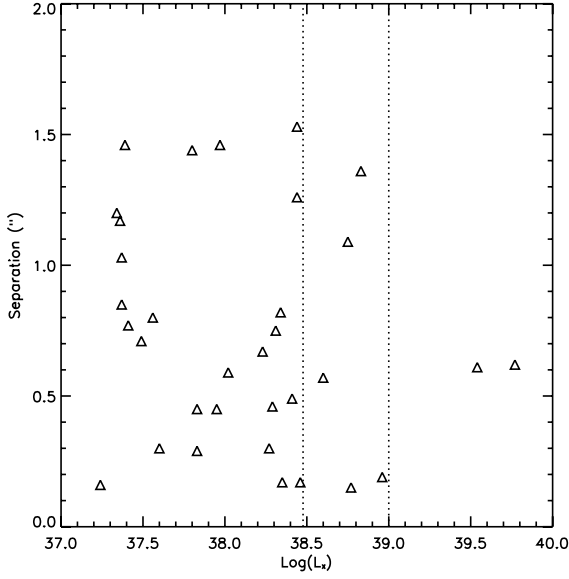


Figure 3. Plot of X-ray luminosity versus separation from the IR counterpart. The dashed lines divide the plot into three separate regions: LLX: $L_X < 3 \times 10^{38} \text{ erg s}^{-1}$, HLX: $3 \times 10^{38} \text{ erg s}^{-1} < L_X < 1 \times 10^{39} \text{ erg s}^{-1}$ and ULX: $L_X > 1 \times 10^{39} \text{ erg s}^{-1}$. Note that there is no trend in X-ray luminosity, nor luminosity class, in terms of separation from an IR counterpart.

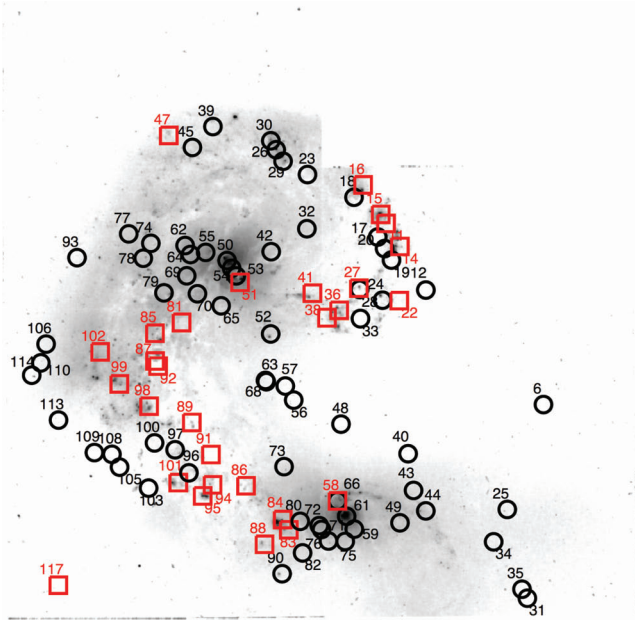


Figure 4. *I*-band Antennae *HST* image showing positions of X-ray sources from Zezas et al. (2006). North is up and east is to the left-hand side. Red squares are optical counterparts to X-ray sources with IR cluster counterparts identified in this paper. Black circles are those X-ray sources lacking cluster counterparts.

To estimate the strength of this result, we performed a χ^2 test between the mean value of η and a fitted line to the plotted values of η (Fig. 6; see Clark et al. 2008). We found a $\Delta\Sigma\chi^2 = 0.45$. Since any value of $\Delta\Sigma\chi^2$ less than one indicates no significant slope, this suggests there is no slope in η . This differs from the value of $\Delta\Sigma\chi^2 = 1.9$ when using only the 15 clusters found with associations to X-ray sources (Clark et al. 2008) and seems to

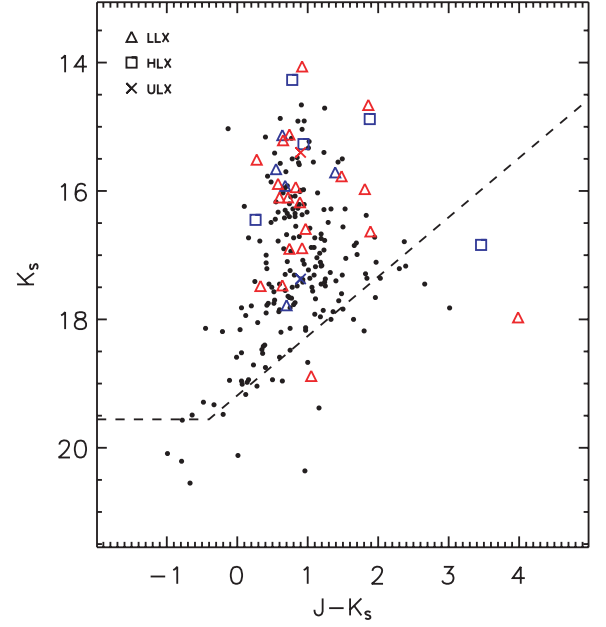


Figure 5. $(J - K_s)$ versus K_s CMD for all clusters in Antennae. Clusters with X-ray sources are designated by the luminosity class of the associated X-ray source. LLX: $L_X < 3 \times 10^{38} \text{ erg s}^{-1}$, HLX: $3 \times 10^{38} \text{ erg s}^{-1} < L_X < 1 \times 10^{39} \text{ erg s}^{-1}$ and ULX: $L_X > 1 \times 10^{39} \text{ erg s}^{-1}$. Blue clusters with X-ray sources are from Clark et al. (2007), while red clusters with X-ray sources are the additional sources added in this work. The dashed line signifies the photometric cut-off we set for statistical purposes.

Table 2. Summary of potential IR counterpart properties. $\sigma_{\bar{K}_s}$ and $\sigma_{(J-K_s)}$ are uncertainties in each value.

| Category | \bar{K}_s | $\sigma_{\bar{K}_s}$ | $(J - K_s)$ | $\sigma_{(J-K_s)}$ |
|---------------|-------------|----------------------|-------------|--------------------|
| All clusters | 16.85 | 0.08 | 0.83 | 0.03 |
| X-ray sources | 16.13 | 0.19 | 1.09 | 0.14 |
| LLX | 15.60 | 0.66 | 1.00 | 0.15 |
| HLX | 15.54 | 0.48 | 1.46 | 0.56 |
| ULX | 16.39 | 0.62 | 0.90 | 0.01 |

strengthen the case that there is only a flat slope in the functional form of $\eta(M_c)$.

3.2 Spectral evolutionary models

During our spectrophotometric analysis of cluster properties, we fitted models to cluster colours across all six IR and optical bands. We estimated cluster colours by performing photometry using the same-sized aperture across all bands. We defined a constant photometric aperture as $\sim 3\sigma$ of the *J*-band Gaussian point spread function (PSF), where the full width at half-maximum (FWHM) is 1.2 arcsec. The background annulus had a radius of $\sim 6\sigma$ – 10σ of the PSF. Considering *HST* resolved many of the IR sources into multiple components, this large photometric aperture encompassed these conglomerations. Since we expect that these sources are part of the same, larger structure, it is appropriate to include photometry of them in spectral evolutionary models.

A bright, Two Micron All Sky Survey (2MASS) star was used to compute *J* and K_s magnitudes (Brandl et al. 2005). We derived *HST* magnitudes using zero-points listed in table 28.1 of the *HST* Data Handbook (Voit 1997). Applying colour transformations defined

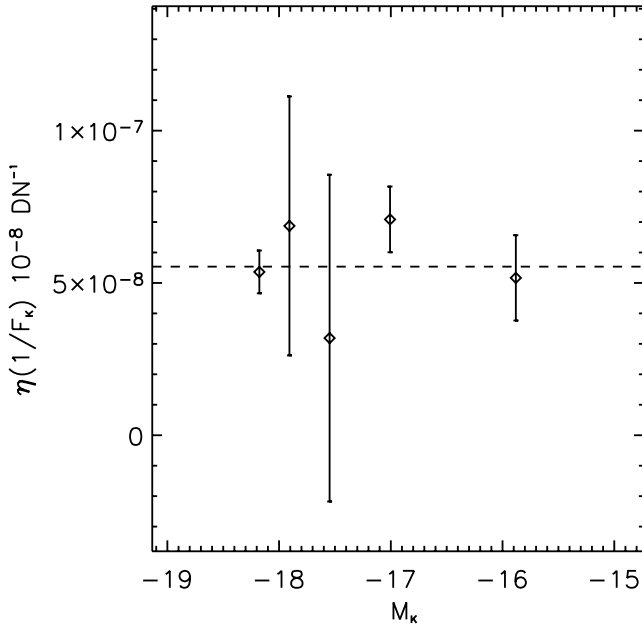


Figure 6. This figure displays $\eta(F_{K_s})$ plotted versus M_{K_s} . The bins are $F_{K_s} = 4.1 \times 10^6 \text{ DN}^{-1}$ in size. Error bars are the uncertainties in the mean value of η added in quadrature with the Poisson uncertainty in each bin. The dotted line is the mean of the five $\eta(F_{K_s})$ values.

in Holtzman et al. (1995), we converted all *HST* magnitudes to Johnson *UBVI* magnitudes. We expressed errors in magnitude, σ_m , as σ_{flux} divided by the mean flux. In the case of the optical filters, σ_m consists of the additional errors in the zero-point and colour transformations, all of which were added in quadrature.

After performing photometry on all X-ray source counterparts seen across all IR and optical bands, we eliminated six sources suffering from poor sky subtraction due to crowding, thus resulting in negative flux measurements. Therefore, we continued further analysis on 21 counterparts to X-ray sources. Performing a χ^2 minimization technique, we fitted Bruzual–Charlot (BC; Bruzual & Charlot 2003) spectral evolutionary models to the cluster magnitudes available for each source to determine mass and age. We fixed the metallicity to $Z = 0.02$, which is an accepted value for young clusters in the Antennae (Christopher 2008; Bastian et al. 2009). These parameters gave us a more complete understanding of the XRB environments in the Antennae. Selecting the model with the best-fitting χ^2 value, we selected all models that had a χ^2 within

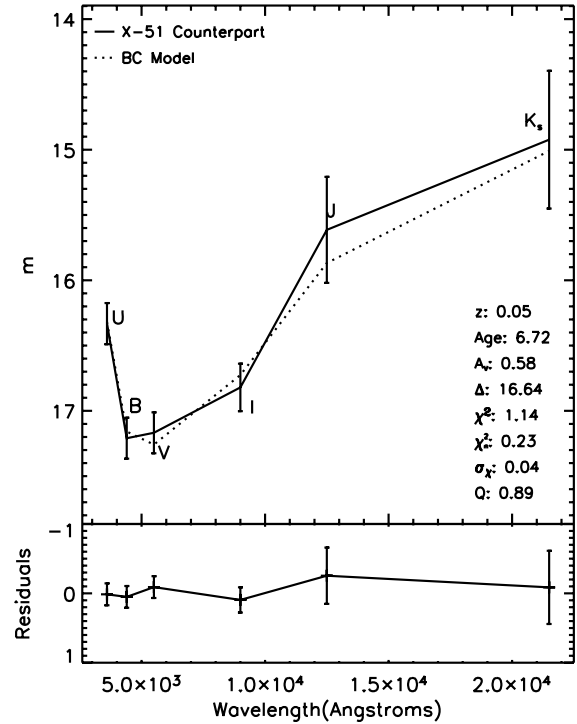


Figure 7. Example of a typical χ^2 fit between a cluster counterpart and a BC model. We include the derived cluster properties and the quality of the fit parameters. Note the small residuals between the model and the data in the lower graph.

one, $\chi^2 + 1$, of these values. The resulting fits gave us a range in age and reddening for each cluster. We estimated reddening by iteratively removing A_V from uncorrected magnitude cluster spectral energy distributions (SEDs). By iteratively picking values for A_V in the range of 0.0–3.0 mag and in steps of 0.1 mag, we selected the A_V that contributed to our best-fitting model. By allowing the value of A_V to float, we accounted for measured uncertainties in reddening. Each fit is listed in Table 3 and an example fit is shown in Fig. 7. We only include those fits with $\chi_n^2 < 1.6$, which is the 1σ confidence interval in χ_n^2 for the number of degrees of freedom in our model fits, $n = 5$. χ_n^2 is equal to χ^2/n .

The shift in magnitude between the model and the data (Δ) gave us a mass estimate for each IR/optical counterpart. Δ contains information on the distance modulus and mass of the cluster. Subtracting off the distance modulus to the Antennae, $m_d = 31.4 \text{ mag}$ (for

Table 3. BC model fits. *Chandra* Src ID numbers follow the naming convention of Zezas et al. (2006). χ_n^2 is the normal χ^2 statistic divided by the degrees of freedom for the fit; five for all filters. Q is a goodness-of-fit measure, showing the probability that χ^2 statistic exceeds a particular value of χ by chance.

| <i>Chandra</i> Src ID | $\text{Log}(L_X)$ | $\text{Log}(\text{age/yr})$ | A_V | $\text{Log}(M/M_\odot)$ | χ_n^2 | Q |
|-----------------------|-------------------|-----------------------------|-----------|-------------------------|------------|------|
| 11 | 38.34 | 6.900–7.477 | 0.94–1.84 | 5.37–6.11 | 0.71 | 0.47 |
| 27 | 39.77 | 7.000–7.477 | 0.98–1.28 | 5.05–5.58 | 0.62 | 0.54 |
| 38 | 38.23 | 7.040–7.440 | 1.04–1.54 | 5.91–6.33 | 0.94 | 0.32 |
| 51 | 38.31 | 6.900–7.360 | 0.48–0.58 | 5.98–6.48 | 0.44 | 0.70 |
| 83 | 38.60 | 6.740–8.306 | 0.70–2.80 | 5.88–7.22 | 0.18 | 0.93 |
| 87 | 37.83 | 6.940–7.420 | 0.71–1.11 | 5.63–6.17 | 0.60 | 0.56 |
| 89 | 37.34 | 7.000–7.477 | 1.48–1.78 | 5.13–5.66 | 0.58 | 0.58 |
| 95 | 38.75 | 7.220–7.360 | 0.71–0.81 | 6.17–6.30 | 1.47 | 0.12 |
| 101 | 38.02 | 7.120–7.160 | 0.45–0.45 | 5.97–5.99 | 1.10 | 0.24 |
| 102 | 37.95 | 6.920–7.440 | 0.35–0.65 | 4.51–5.08 | 1.39 | 0.14 |

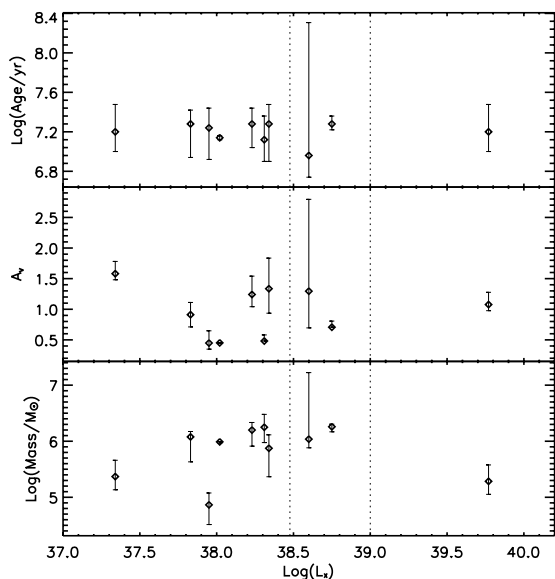


Figure 8. Summary of results from χ^2 fitting to BC models. Error bars are ranges in cluster parameters for models within plus one of the best-fitting χ^2 sum. We divide these plots by X-ray source luminosity into three separate regions: LLX: $L_X < 3 \times 10^{38} \text{ erg s}^{-1}$, HLX: $3 \times 10^{38} \text{ erg s}^{-1} < L_X < 1 \times 10^{39} \text{ erg s}^{-1}$ and ULX: $L_X > 1 \times 10^{39} \text{ erg s}^{-1}$. Note that there is no obvious trend between cluster properties and the luminosity of the associated X-ray source.

$H_0 = 75 \text{ km s}^{-1} \text{ Mpc}^{-1}$), we were left with a difference in luminosity between our cluster and a $1 M_\odot$ cluster as listed by the BC models. Converting this difference into a change in flux gave us the cluster mass in solar masses. Before computing this change in flux, we renormalized the luminosity difference, expressing it in terms of magnitudes instead of colours. We renormalized the luminosity difference to M_{K_s} for all fits, where M_{K_s} was computed using PSF, aperture photometry (see Clark et al. 2007).

We summarize the results from all model fits in Fig. 8. We found ages between $\sim 9 \times 10^6$ – 2×10^7 yr. Masses ranged from 7×10^5 to $2 \times 10^6 M_\odot$, with most $\sim 10^6 M_\odot$. The extinction varied from $A_V = 0.3$ – 1.5 mag. Finally, we did not find a trend between these cluster properties and the luminosities of their associated X-ray sources.

4 CONCLUSIONS

In this work, we made astrometric frame-ties between *Chandra* X-ray coordinates (Zezas et al. 2006), WIRC IR pixel positions and *HST* optical coordinates to search for star cluster counterparts to X-ray point sources. Using the list of 120 X-ray sources in table 3 of Zezas et al. (2006), we found 38 of these sources are associated with an IR counterpart, 35 of which are confirmed star clusters. This expanded on previous work in which we found IR star cluster associations to 15 of the 49 X-ray sources listed in table 1 of Zezas et al. (2002; Clark et al. 2007). Our new sample of IR cluster counterparts includes 11 of the previously identified 15 counterparts discussed in Clark et al. (2007). Both this past study and what we present here indicate that most X-ray sources, roughly two-thirds, do not spatially coincide with a cluster. A comparison between X-ray luminosity and the separation from the associated cluster does not show a trend, thus indicating no relation between XRB type and where it forms in its parent cluster.

Extending our frame-tie from the X-ray to the optical using the IR as an intermediary, we were unable to find reliable optical coun-

terparts due to the crowded *HST* fields. This problem of identifying counterparts to X-ray sources was also encountered in a similar study, which focused on optical counterparts to ULXs (Ptak et al. 2006). Thus, instead, we found the optical counterparts to 27 of the IR star clusters associated with an X-ray source. An examination of the positions of the cluster counterparts in the Antennae indicates that the majority are in the spiral arms and bridge region between these two galaxies. This seems to clearly indicate that those X-ray sources with counterparts are tied to star formation in these interacting galaxies.

Using photometry taken from Brandl et al. (2005), we made an IR, JK_s photometric study of the 33 IR star cluster counterparts whose X-ray sources have listed luminosities. We found most of the IR cluster counterparts are bright, ~ 16 mag in K_s and in slightly redder clusters, $(J - K_s) = 1.1$ mag as compared to $(J - K_s) = 0.8$ mag for the general population of clusters. This confirms our results presented in Clark et al. (2007), in which we performed a similar study with the smaller sample of IR counterparts.

Following the work in Clark et al. (2008), we explored the relationship between cluster mass and the detected number of X-ray sources. In Clark et al. (2008) we defined a function η relating the number of X-ray detections per mass as a function of cluster mass. We found η is consistent with a mean value of $\eta(F_{K_s}) = 5.5 \times 10^{-8}$. Using a χ^2 test, we compared a fitted slope of the plotted $\eta(F_{K_s})$ values to the mean $\eta(F_{K_s})$ value. We found a $\Delta\Sigma\chi^2 = 0.45$. Considering we found a $\Delta\Sigma\chi^2 = 1.9$ in Clark et al. (2008), our new study shows a stronger relation between $\eta(F_{K_s})$ and the mean value, effectively ruling out any inclination towards more X-ray sources residing in more massive clusters other than through simple scaling arguments.

Including the 27 star cluster counterparts to X-ray sources seen across all *UBVIJK_s* bands, we fit BC (Bruzual & Charlot 2003) spectrophotometric models to 10 of these clusters. The BC model fits indicate the X-ray-source-associated clusters are 7×10^5 – $2 \times 10^6 M_\odot$ in mass, $\sim 9 \times 10^6$ – 2×10^7 yr in age, with extinction varying between $A_V = 0.3$ and 1.5 mag. These properties indicate star cluster counterparts to X-ray sources in the Antennae tend to be young and massive, which are consistent with these X-ray sources being associated with star formation. In Ptak et al. (2006), these authors also found similar mass results for their counterparts to ULXs.

While we can use multiwavelength photometry to describe cluster properties, there remains some uncertainty in these characteristics due to errors in magnitude and model limitations. In future work, we plan to acquire spectra of Antennae cluster counterparts and refine estimations of their properties.

ACKNOWLEDGMENTS

The authors thank the staff of Palomar Observatory for their excellent assistance in commissioning WIRC and obtaining these data. WIRC was made possible by support from the NSF (NSF-AST0328522), the Norris Foundation and Cornell University. Based on observations made with the NASA/ESA *HST*, obtained from the data archive at the Space Telescope Science Institute (STScI). STScI is operated by the Association of Universities for Research in Astronomy, Inc. under NASA contract NAS 5-26555. DMC is grateful for the many useful discussions with Michelle Edwards and Valerie Mikles. SSE and DMC received support in part by an NSF CAREER award (NSF-9983830) and an NSF grant (NSF-AST0507547). We also thank J. Houck for his support of the WIRC instrument project.

REFERENCES

- Bastian N., Tranco G., Konstantopoulos I. S., Miller B. W., 2009, *ApJ*, 701, 607
- Brandl B. R. et al., 2005, *ApJ*, 635, 280
- Bruzual G., Charlot S., 2003, *MNRAS*, 344, 1000
- Christopher M. H., 2008, PhD thesis, California Inst. Tech.
- Clark D. M. et al., 2005, *ApJ*, 631, L109
- Clark D. M. et al., 2007, *ApJ*, 658, 319
- Clark D. M. et al., 2008, *ApJ*, 678, 798
- Fabbiano G., 1989, *ARA&A*, 27, 87
- Gehrels N., 1986, *ApJ*, 303, 336
- Holtzman J. A., Burrows C. J., Casertano S., Hester J. J., Trauger J. T., Watson A. M., 1995, *PASP*, 107, 1065
- King A. R., Davies M. B., Ward M. J., Fabbiano G., Elvis M., 2001, *ApJ*, 552, L109
- Lada C. J., Lada E. A., 2003, *ARA&A*, 41, 57
- Makishima K. et al., 2000, *ApJ*, 535, 632
- Ptak A., Colbert E., van der Marel R. P., Roye E., Heckman T., Towne B., 2006, *ApJS*, 166, 154
- Roberts T. P., 2007, *Ap&SS*, 311, 203
- Roberts T. P., Warwick R. S., 2000, *MNRAS*, 315, 98
- Saviane I., Hibbard J. E., Rich R. M., 2004, *AJ*, 127, 660
- Schweizer F. et al., 2008, *AJ*, 136, 1482
- Voit M., 1997, *HST Data Handbook*. STScI, Baltimore
- Whitmore B. C., Zhang Q., Leitherer C., Fall S. M., 1999, *AJ*, 118, 1551
- Zezas A., Georgantopoulos I., Ward M. J., 1999, *MNRAS*, 308, 302
- Zezas A., Fabbiano G., Rots A. H., Murray S. S., 2002, *ApJ*, 142, 239
- Zezas A., Fabbiano G., Baldi A., Schweizer F., King A. R., Ponman T. J., Rots A. H., 2006, *ApJS*, 166, 211

This paper has been typeset from a $\text{\TeX}/\text{\LaTeX}$ file prepared by the author.